

**Ab initio calculation of the shock Hugoniot of bulk silicon**

Oliver Strickson\*

*Cavendish Laboratory, University of Cambridge, J. J. Thomson Avenue, Cambridge CB3 0HE, United Kingdom*

Emilio Artacho

*Theory of Condensed Matter, Cavendish Laboratory, University of Cambridge, J. J. Thomson Avenue, Cambridge CB3 0HE, United Kingdom;**CIC Nanogune and DIPIC, Tolosa Hiribidea 76, 20018 San Sebastián, Spain;**and Basque Foundation for Science Ikerbasque, Bilbao, Spain*

(Received 6 July 2015; revised manuscript received 18 February 2016; published 17 March 2016)

We describe how *ab initio* molecular dynamics can be used to determine the Hugoniot locus (states accessible by a shock wave) for materials with a number of stable phases, and with an approximate treatment of plasticity and yield, without having to simulate these phenomena directly. We consider the case of bulk silicon, with forces from density-functional theory, up to 70 GPa. The fact that shock waves can split into multiple waves due to phase transitions or yielding is taken into account here by specifying the strength of any preceding waves explicitly based on their yield strain. Points corresponding to uniaxial elastic compression along three crystal axes and a number of postshock phases are given, including a plastically yielded state, approximated by an isotropic stress configuration following an elastic wave of predetermined strength. The results compare well to existing experimental data for shocked silicon.

DOI: [10.1103/PhysRevB.93.094107](https://doi.org/10.1103/PhysRevB.93.094107)**I. INTRODUCTION**

Shock waves are used extensively to study matter at conditions of extreme pressure and temperature, and have been used to obtain some of the highest laboratory-attained pressures. They are useful for equation of state determination and are important dynamic phenomena in their own right, arising in aerodynamics [1], reactive flow [2], and high-speed impact [3,4].

Simulations of shock waves have a long history [5]. Direct simulations using empirical potentials are now feasible on a multibillion-atom scale on present hardware, which is large enough to observe detailed mechanisms of yield, plastic flow, and shock interaction with nanostructures directly [6,7]. Work with empirical potentials can give important insight and understanding, but a need for first-principles methods such as density-functional theory (DFT) exists in providing predictive power and accuracy. These methods must use more modest system sizes, of hundreds or thousands of atoms in the case of DFT.

Several approaches can be taken for the determination of a Hugoniot locus from molecular dynamics. The most straightforward, but computationally the most demanding, is to simulate a slab of atoms struck by an impactor directly, measuring the speed of any shock waves and postshock average particle velocities as they arise from the simulation. From the Hugoniot relations, these velocities can be converted to a relationship between pressure and volume compression. For empirical potentials, a local stress is conveniently available, so this could also be taken directly from the simulation. This is the approach taken by, e.g., Kadau *et al.* [8].

It is simple to check that a given equilibrium state lies on or close to the (single-shock) Hugoniot locus, which amounts

to satisfying the Hugoniot relation

$$E - E_0 = \frac{1}{2}(\sigma^{33} + \sigma_0^{33})(v_0 - v), \quad (1)$$

where  $E$  is the specific internal energy,  $v$  is the specific volume, and  $\sigma^{33}$  is the stress in the direction of the shock (and can be replaced with the pressure  $p$  in a hydrostatic situation). We use the convention that stress is positive under compression. The zero-subscripted variables are for the preshocked state. Other (equivalent) Hugoniot relations exist between any three of the internal energy, pressure, volume, shock velocity, and particle velocity. It is therefore sufficient to sample several points that are chosen to bracket the Hugoniot locus, and the Hugoniot state is then approximated by interpolation, or solved for iteratively. The former is the approach taken by Bonev *et al.* [9] for shocked DFT deuterium. Phase transitions are observed if they occur spontaneously in the simulation.

Alternatively, a Hugoniot state can be determined dynamically from within a single molecular dynamics simulation by some modified dynamics to constrain the state to satisfy Eq. (1). This is the approach taken by the Hugoniotstat methods [10,11] and the technique of Reed *et al.* [12]. The former simulations use modified Nosé-Hoover dynamics while the latter uses coupled dynamics of the atoms and simulation cell, whose Lagrangian involves the computed instantaneous shock speed, and varies the simulation cell uniaxially. One aim of these dynamics is to work on time scales comparable to shock-passage times, without the overhead of dealing with a direct nonequilibrium simulation. These have been used successfully with empirical potentials, but also first-principles forces [13].

If we are interested only in the final postshock state, and are not interested in the (modified) dynamics while the constraint is being applied, we are free to use a method based on simple velocity rescaling, analogous to the procedure of Berendsen [14], which is what we use here due to its increased efficiency in reaching the final state, and to avoid

\*ots22@cam.ac.uk

large oscillations when starting far from the target state. This alternative approach was also taken by Mattsson *et al.* [15] and Taylor [16].

Shocks to stresses above the the elastic regime can show plasticity and yield, as well as phase transitions (either to other solid phases or to a liquid). These effects are challenging to represent by any method. A small simulation is likely to show large hysteresis in the case of phase transitions, and vastly overestimated yield stress. When plastic yielding does occur, it can exhibit artefacts due to the limited size or artificial periodicity that dominate the desired effect. In addition, this introduces an additional time scale that can be much longer than we would otherwise need to run a simulation without yielding, or in a single phase.

The approach we propose here is to avoid simulations containing explicit yielding or phase transitions, and instead focus on specifying the final structure, which at a given shock strength determines the Hugoniot state uniquely via Eq. (1). In the case of a yielded state, we can approximate this in the following way. A shock wave results in a uniaxial strain on the material, and the material yields as a means to reduce the deviatoric stress, resulting in a close-to-hydrostatic stress. We can therefore approximate the final state as being due to a strain on the original structure that results in hydrostatic stress, while also satisfying Eq. (1). This allows small simulations for short times to capture multiple phases and plasticity, which would otherwise need much larger and longer simulations.

Silicon has a rich phase diagram, with metallic dense phases rather different in character from the ambient diamond phase, making it an interesting and challenging object of simulation. In total, 11 stable or metastable phases of silicon are currently known [17]. Shock experiments have provided important data for constructing the phase diagram. The phase transition in silicon from the cubic diamond structure to the  $\beta$ -tin structure, occurring at 12 GPa at room temperature, and undergoing a reduction in volume of 20%, has been well established by static loading experiments from the 1960s onward [18,19]. Evidence of at least one phase transition at similar pressures was then observed in shock-wave experiments, starting with Pavlovskii [20].

If a shock wave is strong enough to cause a material to yield plastically or undergo a phase transition, the wave can split into two or more separate shock waves, and this has long been observed and understood [3]. In this situation, the last shock takes the material to its final state, but the preceding shocks take the material to a cusp on the pressure-volume Hugoniot locus caused by a transition: either the Hugoniot elastic limit or the onset pressure of a phase transition. In silicon, Gust and Royce [21,22] found a three-wave structure for samples shocked in the  $\langle 100 \rangle$  crystal direction and a four-wave structure when shocked in the  $\langle 110 \rangle$  or  $\langle 111 \rangle$  direction. In the latter cases, these waves were attributed to an initial elastic precursor to the Hugoniot elastic limit of 5.5 GPa, followed by waves corresponding to a state of plastic yield and two successive phase transitions at 10 GPa and 13 GPa. Along  $\langle 100 \rangle$ , the higher elastic limit of 9 GPa obscures the first transition wave, and a single wave takes the material simultaneously to a new phase and to a state of hydrostatic stress.

The work of Goto *et al.* [23] largely confirmed the findings of Gust and Royce [22], although they observed a three-wave

structure, regardless of crystal orientation, consistent with only a single phase transition at 13 GPa. Above the Hugoniot elastic limit, shock compression was found to result in a hydrostatic stress configuration, due to the complete loss of strength in the material.

More recently, and contrary to the earlier experimental work, Turneure and Gupta [24,25] reported a single phase transition that is complete by 15.9 GPa. Shocks to these pressures show a much greater volume compression than the points attributed to an extended mixed-phase region by both Gust and Royce [22] and Goto *et al.* [23]. Here the phase transition is not complete until at least 30 GPa. This discrepancy is explained by Turneure and Gupta [25] as arising from the reflection of the first two shock waves propagating back into the material before the arrival of the third wave, and altering the peak state of the earlier experiments. They avoid this eventuality by backing the silicon with a window made from lithium fluoride, a material with a good impedance match to silicon.

The *Imma* phase of silicon is found intermediate between the  $\beta$ -tin and simple hexagonal phases, and is stable between 13 GPa and 15 GPa at room temperature [26]. Theoretically, the energy and volume of these three phases are close [17]. A recent simulation of directly shocked silicon using an empirical potential [27] found a phase transition to an *Imma* phase with a modification of the Tersoff potential [28,29] of Erhart and Albe [30].

In this paper, we give the Hugoniot loci according to density-functional theory for several pure phases of silicon, including cubic diamond under elastic compression along  $\langle 100 \rangle$ ,  $\langle 110 \rangle$ , and  $\langle 111 \rangle$ , a hydrostat (resulting from either a single shock or a split-shock structure),  $\beta$ -tin, simple hexagonal, and the liquid, and report shock temperatures for these states. The agreement is good overall. The picture that emerges from calculations is that Hugoniot locii for the  $\beta$ -tin and simple hexagonal phases from the same (cubic diamond) starting state are very close, but that the simple hexagonal results are more consistent with experiment.

## II. COMPUTATIONAL METHOD

### A. Density-functional theory

The *ab initio* MD simulations described here were performed with the SIESTA method and implementation of density-functional theory [32], using the Perdew *et al.* [33] generalized gradient approximation functional. The core electrons were described with a Troullier-Martins norm-conserving pseudopotential [34] with a matching radius in each angular momentum channel of  $1.89a_0$ . The valence electrons were described with a basis of numerical atomic orbitals of double- $\zeta$  polarized type [31] (representing 13 orbitals per atom). The basis was generated by fixing the longest orbital cutoffs at  $7.0a_0$  and variationally optimizing the other parameters in bulk diamond-phase silicon—the final basis parameters are given in Table I.

The mesh used for integrals in real space was well converged at a grid cutoff of 100 Ry. The dense phases of silicon required several  $k$  points to converge in energy, and, in particular, for the cold compression curves of the various

TABLE I. Basis parameters for silicon, according to the soft-confinement scheme of Junquera *et al.* [31]. For the purposes of basis generation, an effective ionic charge of  $-0.46$  was used, which was also variationally optimized. The cutoff radii of the first and second zeta functions are  $r(\zeta_1)$  and  $r(\zeta_2)$ , and  $r_i$  is the confinement potential's internal radius.  $V_0$  is the soft-confinement prefactor.

$n$	$l$	$r_i (a_0)$	$r(\zeta_1) (a_0)$	$r(\zeta_2) (a_0)$	$V_0$ (Ry)
3	0	4.97	7.00	4.38	15.43
3	1	3.83	7.00	4.09	4.70
3	2	0.03	4.55		11.97

phases to converge in energy relative to one another. A  $4^3$  Monkhorst-Pack grid of points was used on the 64-atom simulations, to give an effective cutoff length of 21 Å.

The electronic temperature used in the DFT calculations should be consistent with the final temperature attained after the annealing process described below. The consistent forces for the *ab initio* molecular dynamics are the nuclear-position derivatives of the electronic free-energy as defined in Mermin's DFT [35]. All of the simulations reported below are for an electronic temperature of 300 K, except for the two points with highest temperatures, for which the electronic temperature was adjusted to coincide with the final (nuclear) temperature. The effect of the electronic temperature on the reported quantities was found to be quite small: the maximum difference in pressure for the hottest simulation between using a consistent electronic temperature and the initial 300 K is below 5%.

### B. Annealing to the Hugoniot locus

We use an annealing procedure to find the state on the Hugoniot corresponding to a specified longitudinal strain. A Berendsen thermostat [14] is used with a variable target temperature computed from the instantaneous difference in energy between the total energy of the system and the total energy that would be required to satisfy the energy Hugoniot relation, Eq. (1), exactly, given the current instantaneous longitudinal stress.

This may be combined with a further anneal to relax the pressure to a hydrostatic configuration if desired. Optionally, the box vectors may be gradually ramped between two states, which is most useful when the starting state of the simulation and the initial state of the Hugoniot locus are the same.

As with Mattsson *et al.* [15] and Taylor [16] we use a modified Berendsen thermostat, instead of a modified Nosé-Hoover, to avoid large initial oscillations. Even though Berendsen thermo- and barostats do not reproduce canonical statistics [36], we are interested only in the outcome of the anneal, not the intermediate dynamics. After the time-averaged state of the system closely satisfies the Hugoniot relation, the simulation can be restarted with Verlet dynamics to check if Eq. (1) is indeed satisfied. The integration of the dynamics used the Born-Oppenheimer approximation with a time step of 1 fs.

To find the Hugoniot for a state after a structural phase transition, the starting structure for the anneal is the postshock phase, but importantly, the “zero” state ( $E_0$ ,  $\sigma_0^{33}$ , and  $v_0$ ) appearing in Eq. (1) is for the initial, preshocked phase. It

is reasonable to keep a hydrostatic stress distribution in the final state. The way to treat plasticity is similar, and is detailed and exemplified in the Results section.

The specific volume at zero stress and 300 K for the PBE functional is  $0.421 \text{ cm}^3/\text{g}$ , which is smaller than the experimental value of  $0.431 \text{ cm}^3/\text{g}$ . The reduced volume is plotted in the figures: if the specific volume were plotted instead, the DFT results would be offset by an amount corresponding to the difference in zero-stress volume. Both the particle velocity and shock velocity are therefore underestimated by a factor of approximately  $\sqrt{0.431/0.421}$ , or 1%.

### III. RESULTS

The calculated stress–volume and shock-velocity–particle-velocity Hugoniot loci for the pure phases are compared with results from several experiments in Figs. 1–3. The curves for the elastic shocks are computed from a uniaxial box deformation along the indicated direction. The “plastic” curve is for a split shock, with an elastic precursor to 9 GPa, taking the material to a hydrostatic stress configuration. This supposes that the material has no residual strength: after the first, elastic wave has passed, it cannot support any deviatoric stress. A split shock wave in general satisfies the combined jump condition [Eq. (1)] from both waves, giving

$$E - E_0 = \frac{1}{2}(\sigma_1^{33} + \sigma_0^{33})(v_0 - v_1) + \frac{1}{2}(\sigma^{33} + \sigma_1^{33})(v_1 - v) \quad (2)$$

for a two-wave split, where the state labeled “1” is the state after the first shock, but before the second, and for a three-wave

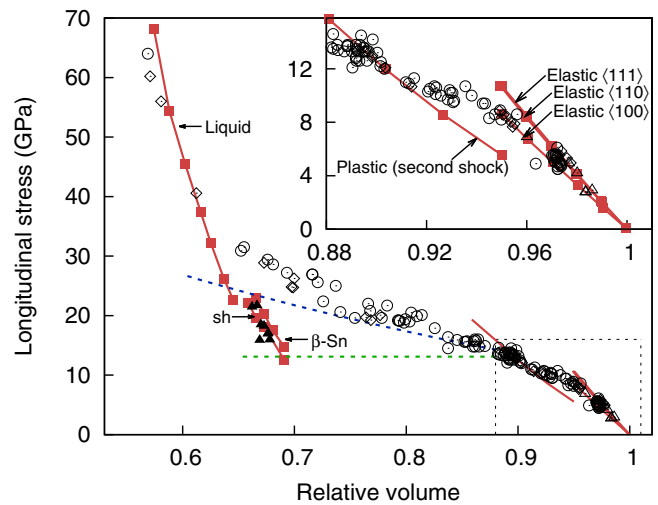


FIG. 1. Longitudinal stress–volume Hugoniot loci for silicon. The red lines in the figure are the DFT results from this work (with contained points indicating individual simulations), with an initial preshocked state of zero pressure and 300 K, with the final state in the indicated phase (“sh” for simple hexagonal). Estimated error is less than 5% for the liquid and  $\beta$  phases, and is substantially smaller for the diamond phase, at under 1%. The symbols are experimental results from the literature:  $\circ$  Gust and Royce [22],  $\diamond$  Goto *et al.* [23],  $\Delta$  Turneure and Gupta [24],  $\blacktriangle$  Turneure and Gupta [25]. The dashed lines are approximations to the mixed-phase portion of the Hugoniot, for cubic diamond to  $\beta$ -tin (green) and liquid (blue).

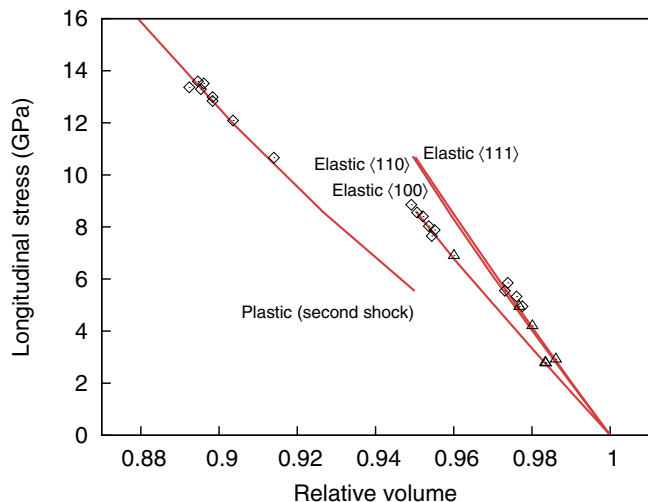


FIG. 2. Longitudinal stress–volume Hugoniot loci for silicon. This is a similar plot to Fig. 1, with the meaning of the symbols and lines the same, emphasizing the small-strain region of the Hugoniot locus and with the results of Gust and Royce [22] omitted due to their larger variance.

split, by

$$E - E_0 = \frac{1}{2}(\sigma_1^{33} + \sigma_0^{33})(v_0 - v_1) + \frac{1}{2}(\sigma_2^{33} + \sigma_1^{33})(v_1 - v_2) + \frac{1}{2}(\sigma^{33} + \sigma_2^{33})(v_2 - v) \quad (3)$$

with the state labeled “2” after the second shock, but before the third. The volume collapse due to the discrete change in model from uniaxial to isotropic compression at the Hugoniot elastic limit is 2% for shocks in the  $\langle 100 \rangle$  direction and 2.5% in the  $\langle 110 \rangle$  and  $\langle 111 \rangle$  directions. The energy rise in this simulation

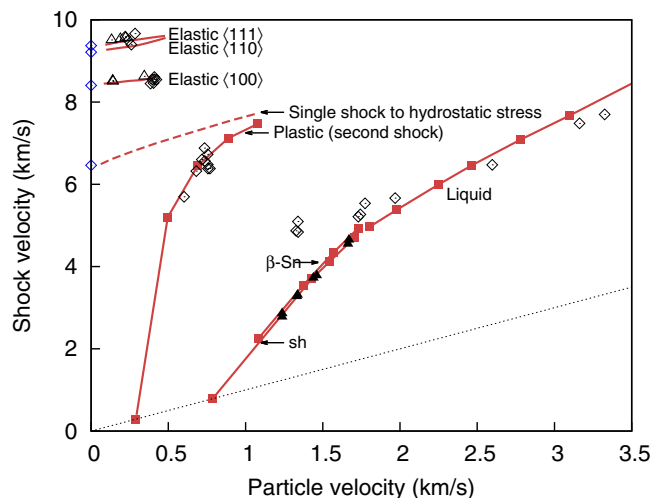


FIG. 3. Particle velocity–shock velocity Hugoniot loci for silicon. The DFT results (red lines and points) each correspond to an initial state of zero stress and 300 K, with the final state in the indicated phase. The dashed line is for a single-shock process whose final state has a hydrostatic stress configuration. The meaning of the symbols is the same as in Fig. 1, with the blue diamonds elastic (highest three points) and bulk wave speeds (lowest point) from Goto *et al.* [23]. The dotted baseline indicates equal shock and particle velocity, below which no viable shock should be recorded.

is due to this volume collapse alone, since we do not include dissipative effects (such as the motion or production of dislocations), or any volume change due to the formation of these defects. It is not beyond the technique, but knowledge of an accurate final structure with the correct distribution of defects would be needed. A description of the processes by which they are formed is not required by the model, however. The final structure determines the energy jump completely, meaning that this contribution is not missing from the liquid simulations, and the missing contribution for the  $\beta$ -tin and simple hexagonal phases is relatively small (due to the much larger volume collapse from the change in structure).

The single-shock hydrostat in Fig. 3 is for an unphysical shock process that relaxes the material to hydrostatic stress behind a single, unsplit shock wave, satisfying the single-shock Hugoniot relation Eq. (1), instead of the physical two-shock Hugoniot relation Eq. (2), seen to agree well with experiment. The single-shock Hugoniot permits comparison with the bulk speed of sound (the shock velocity for this wave should extrapolate to the bulk speed of sound at zero particle velocity), and this agreement can also be seen in Fig. 3 to be good.

The agreement in Fig. 3 between our calculations and the experimental data for the elastic and plastic shocks is good, with the compressibility along each direction matching well. The close match between the experimental plastic shock stresses and the hydrostatic plastic shock calculated here (for the two-shock process) supports the observation that the material loses all of its strength after yield.

The particle and shock velocities in Fig. 3 are computed from the computed stress and volume points using the Hugoniot relations

$$u_p^2 = (\sigma^{33} - \sigma_0^{33})(v_0 - v), \quad (4)$$

$$U_s^2 = v_0^2(\sigma^{33} - \sigma_0^{33})/(v_0 - v) \quad (5)$$

for the single-shock case,

$$u_p = \sqrt{(\sigma^{33} - \sigma_1^{33})(v_1 - v)} + \sqrt{(\sigma_1^{33} - \sigma_0^{33})(v_0 - v_1)}, \quad (6)$$

$$U_s = v_0 \sqrt{(\sigma^{33} - \sigma_1^{33})/(v_1 - v)} + \sqrt{(\sigma_1^{33} - \sigma_0^{33})(v_0 - v_1)} \quad (7)$$

for the two-wave split-shock case, and

$$u_p = \sqrt{(\sigma^{33} - \sigma_2^{33})(v_2 - v)} + \sqrt{(\sigma_2^{33} - \sigma_1^{33})(v_1 - v_2)} + \sqrt{(\sigma_1^{33} - \sigma_0^{33})(v_0 - v_1)}, \quad (8)$$

$$U_s = v_0 \sqrt{(\sigma^{33} - \sigma_2^{33})/(v_2 - v)} + \sqrt{(\sigma_2^{33} - \sigma_1^{33})(v_1 - v_2)} + \sqrt{(\sigma_1^{33} - \sigma_0^{33})(v_0 - v_1)} \quad (9)$$

for the three-wave split-shock case. Linear fits to the elastic part of the shock-velocity–particle-velocity Hugoniot, for experiment (computed by the original authors) and for our computed results, have coefficients given in Table II. The extrapolated value of the bulk sound speed of 6.51 km/s agrees very well with the value of 6.48 km/s calculated from the second-order elastic constants [22,37].

TABLE II. Coefficients of a linear fit of the shock velocity for the elastic waves,  $U_s = c_0 + su_p$ , for this work and two sets of experimentally determined values.

	$\langle 100 \rangle$		$\langle 110 \rangle$		$\langle 111 \rangle$		Bulk	
	$c_0$ (km/s)	$s$ (dimensionless)	$c_0$	$s$	$c_0$	$s$	$c_0$	$s$
This work	8.38	0.42	9.21	0.57	9.34	0.57	6.51	1.18
Ref. [23]	8.42	0.32	9.24	1.01	9.39	0.98		
Ref. [37]	8.43		9.13		9.34 <sup>a</sup>		6.48 <sup>a</sup>	

<sup>a</sup>Calculated from the given elastic constants and density.

The  $\beta$ -Sn and simple hexagonal curves each correspond to a three-wave split-shock structure, behind an elastic wave in the  $\langle 100 \rangle$  direction to the experimental elastic limit of 9 GPa according to Turneure and Gupta [25] and a secondary wave to the approximate location of the phase transition, at 13.8 GPa. We evaluated the plastic Hugoniot at several discrete points, and this was the closest to the experimental transition pressure, given as 13.4(2) GPa by Goto *et al.* [23] and as 14.0(40) GPa by Gust and Royce [22]. For both of these waves, the computed volume for the  $\langle 100 \rangle$  direction was used for the postshock state. The values of volume, pressure, and energy differences when the wave splits are summarized in Table III. The second and third shock Hugoniot loci are quite insensitive to the precise location of the wave splits, particularly the elastic-plastic split, since the contribution to the energy change is much smaller than the 20% volume reduction across the phase change. The final stress was hydrostatic. Since the  $c/a$  ratio is free in the  $\beta$ -Sn and simple hexagonal structures, an additional relaxation step was used on the simulation box to impose a hydrostatic distribution of stress while simultaneously annealing to the Hugoniot. The  $\beta$ -Sn and simple hexagonal curves are close in pressure, temperature and shock velocity, with the experimental values closest to the simple hexagonal DFT Hugoniot. The computed pressures and temperatures of these points put them in the stable region for the simple hexagonal structure on the silicon phase diagram [38].

Part of the liquid Hugoniot corresponds to a three-wave shock structure, with the third wave reaching the final liquid state, behind a secondary wave to the onset of the melting transition and an elastic precursor wave. For the highest pressures, where the final wave has a velocity greater than that of the secondary wave of 6.83 km/s, it instead corresponds to a two-wave structure (behind only the elastic precursor). The largest shock pressures closely match the calculated liquid Hugoniot, with the simulated liquid being systematically slightly too stiff, as evidenced by the steeper slope of the liquid curve in Fig. 1 than in experiment.

TABLE III. Summary of the values for the states used at the locations of the wave splitting.

	$v$ (cm <sup>3</sup> /g)	$\sigma^{33}$ (GPa)	$E$ (J/g)
Initial state	0.431	0.0	0.0
First wave to Hugoniot elastic limit, (100) direction	0.410	9.0	94.5
Second wave to phase transition onset	0.384	13.8	390.9

The predicted postshock temperatures are given in Fig. 4. This clearly indicates that the highest pressure points are likely to be in the liquid phase, but that the lowest three points are below the melting point (and so represent a rapidly annealed solid).

### A. The phase transition

There is a considerable range of relative volume between the Hugoniot loci of the pure phases shown in Fig. 1. The experimentally measured points in this region have a final state that is a mixture of two phases. Points on the mixed-phase region of the Hugoniot are on the intersection of the phase boundary for the two phases, as well as satisfying Eq. (1).

Similarly to the plastic shock, a pressure-volume Hugoniot is convex at the onset of a mixed phase region: if the change in slope is great enough, this causes the shock to split into a wave taking the material to the pressure at the onset of the phase transition, and a slower wave taking the material to its final state, which is a coexistence of the two phases.

The Hugoniot locus through the mixed-phase region can be constructed by considering the jump condition in enthalpy across the shock from the point (“1”) at the onset of the

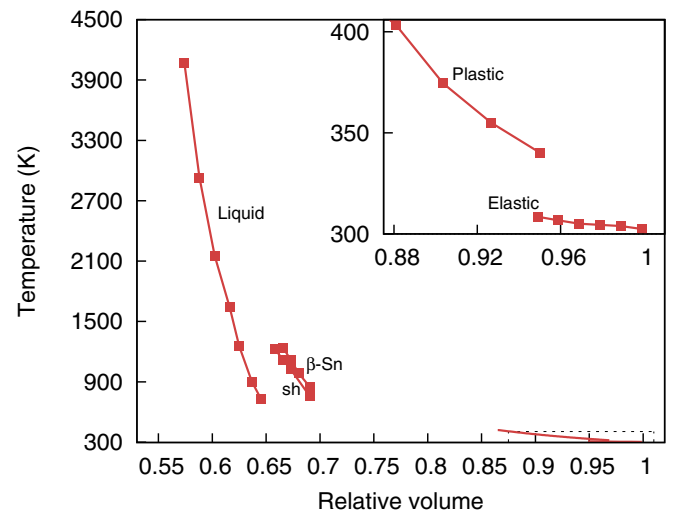


FIG. 4. Postshock temperature as a function of volume for several final states. The DFT results (red lines, solid and dashed) each correspond to an initial state of zero stress and 300 K, with the final state in the indicated phase. The statistical error was at most 3%, worse for the hottest liquid points. The “plastic” curve does not include the temperature rise due to dissipative heating. The meaning of the symbols is the same as in Fig. 1.

TABLE IV. Summary of values used at the onset of the cubic diamond to liquid phase transition. The phase line is as obtained by the experiment of Kubo *et al.* [38]. The other values are from Hull [40], with  $\alpha$  and  $c_p$  at 1600 K and ambient pressure, and  $\beta$  at 298 K and 13.8 GPa.

$T$ (K)	$dT/dP$ (K GPa $^{-1}$ )	$\alpha$ (K $^{-1}$ )	$\beta$ (GPa $^{-1}$ )	$c_p$ (J g $^{-1}$ K $^{-1}$ )
1683	62.4	$4.5 \times 10^6$	0.024	1.0

transition to a point (“2”) on the mixed Hugoniot

$$h_2 - h_1 = E_2 - E_1 + p_2 v_2 - p_1 v_1, \quad (10)$$

and on substituting Eq. (1) for the jump in internal energy, this reduces to

$$h_2 - h_1 = \frac{1}{2}(p_2 - p_1)(v_2 + v_1). \quad (11)$$

The latent heat  $L$  of the phase transition results in a change in enthalpy, written according to the Clausius–Clapeyron equation as

$$\lambda L = -T(dp/dT)(v_1 - v_2), \quad (12)$$

where  $\lambda$  is the mass fraction of the second phase and the derivative is along the phase line.

Since the mixed region is not at constant pressure, there is an additional contribution to the enthalpy change from the difference in pressure and volume between the onset of the transition and the postshock state. This leads to a linearized equation relating the pressure and volume changes on the phase-transition shock [39],

$$p_2 - p_1 = (v_1 - v_2) \left[ \beta v_1 + \left( \frac{1}{2T_1}(v_1 - v_2) - 2\alpha v_1 \right) \times \frac{dT}{dp} + \frac{c_p}{T_1} \left( \frac{dT}{dp} \right)^2 \right]^{-1}, \quad (13)$$

where  $\beta$  is the isothermal compressibility,  $\alpha$  is the volumetric thermal expansion coefficient, and  $c_p$  is the specific heat capacity at constant pressure. The derivative  $dT/dp$  is once again along the phase boundary.

We require knowledge of the onset of the transition in the  $p$ - $v$  plane, which is not available from the single-phase simulations alone (the simulated materials are capable of being substantially superheated or supercooled). This could be obtained from the point where the Hugoniot cuts the phase boundary obtained by some other method.

We consider here two possible phase transitions starting from silicon in the cubic diamond structure: to a liquid, and to the  $\beta$ -tin structure. For the purpose of determining the intermediate state in (2), we approximate the onset of the transition in DFT silicon by 13.8 GPa, as already described. The phase lines are experimental values, obtained by Kubo *et al.* [38]. This gives the two dashed lines appearing in Fig. 1. The green dashed line for the transition from diamond

structure to  $\beta$ -tin is nearly at constant pressure, since its slope is dominated by the steep phase line of the transition [38]  $dT/dp = -1426$  K/GPa. This is consistent with the experiment of Turneure and Gupta [25]. The blue dashed line for melting the diamond structure is influenced most strongly by the compressibility  $\beta$  of the cubic diamond phase at the pressure and temperature of the onset. Representative literature values for the constants appearing in the above expression for the liquid are summarized in Table IV. This line underestimates the experimentally observed slope seen by Gust and Royce [22] and Goto *et al.* [23]. While the simulated temperature at this pressure is much too low for melting, the simulations of the “plastically yielded” state do not include dissipative heating and this could cause a significant further temperature rise above those reported in Fig. 4.

#### IV. CONCLUSION

In conclusion, we have described how to use first-principles calculations to find the Hugoniot locus of several phases of silicon using an annealing method, allowing the locus through the pure phases to be found without relying on spontaneous phase transitions occurring within the molecular dynamics simulation. An approximation relying on the slope of the phase boundary can be used to obtain the part of the Hugoniot corresponding to coexistence between two phases. Under the assumptions made here concerning plasticity and phase transitions, along with accurate first-principles calculations, good agreement with experiment is achieved.

The results computed using this procedure with the forces described using density-functional theory match existing experimental data very well for pressures up to 60 GPa, the limit of available experimental data. We have provided a prediction of the shock temperatures of silicon over this pressure range. This study supports the conclusions of the experimental work in general, that silicon after yield supports no deviatoric stress, and of Turneure and Gupta [25] that the first observed phase transition along the shock locus is likely to be to simple hexagonal.

#### ACKNOWLEDGMENTS

We thank Alan Minchinton, Richard Needs, Nikos Niki-forakis, Stephen Walley and David Williamson for useful input and discussions. This research was supported with funding from Orica Ltd. and the following grants: MINECO-Spain’s Plan Nacional Grant No. FIS2012-37549-C05-01, Basque Government Grant No. PI2014-105 CIC07 2014-2016, and EU Grant “ElectronStopping” in the Marie Curie CIG Program. Part of this work was performed using the Darwin Supercomputer of the University of Cambridge High Performance Computing Service [41], provided by Dell Inc. using Strategic Research Infrastructure Funding from the Higher Education Funding Council for England and funding from the Science and Technology Facilities Council.

[1] D. S. Dolling, *AIAA J.* **39**, 1517 (2001).

[2] D. D. Dlott, *Ann. Rev. Phys. Chem.* **62**, 575 (2011).

[3] G. E. Duvall and R. A. Graham, *Rev. Mod. Phys.* **49**, 523 (1977).

[4] J. Asay and M. Shahinpoor (eds.), *High-Pressure Shock Compression of Solids*, Shock Wave and High Pressure Phenomena (Springer-Verlag, New York, 1993).

- [5] B. Holian, *Shock Waves* **13**, 489 (2004).
- [6] K. Kadau, T. C. Germann, and P. S. Lomdahl, *Int. J. Mod. Phys. C* **17**, 1755 (2006).
- [7] A. Shekhar, K.-i. Nomura, R. K. Kalia, A. Nakano, and P. Vashishta, *Phys. Rev. Lett.* **111**, 184503 (2013).
- [8] K. Kadau, T. C. Germann, P. S. Lomdahl, R. C. Albers, J. S. Wark, A. Higginbotham, and B. L. Holian, *Phys. Rev. Lett.* **98**, 135701 (2007).
- [9] S. A. Bonev, B. Militzer, and G. Galli, *Phys. Rev. B* **69**, 014101 (2004).
- [10] J.-B. Maillet, M. Mareschal, L. Soulard, R. Ravelo, P. S. Lomdahl, T. C. Germann, and B. L. Holian, *Phys. Rev. E* **63**, 016121 (2000).
- [11] R. Ravelo, B. L. Holian, T. C. Germann, and P. S. Lomdahl, *Phys. Rev. B* **70**, 014103 (2004).
- [12] E. J. Reed, L. E. Fried, and J. D. Joannopoulos, *Phys. Rev. Lett.* **90**, 235503 (2003).
- [13] S. Bernard and J. B. Maillet, *Phys. Rev. B* **66**, 012103 (2002).
- [14] H. J. C. Berendsen, J. P. M. Postma, W. F. van Gunsteren, A. DiNola, and J. R. Haak, *J. Chem. Phys.* **81**, 3684 (1984).
- [15] T. R. Mattsson, J. M. D. Lane, K. R. Cochrane, M. P. Desjarlais, A. P. Thompson, F. Pierce, and G. S. Grest, *Phys. Rev. B* **81**, 054103 (2010).
- [16] D. E. Taylor, *J. Am. Ceram. Soc.* **98**, 3308 (2015).
- [17] A. Mujica, A. Rubio, A. Muñoz, and R. J. Needs, *Rev. Mod. Phys.* **75**, 863 (2003).
- [18] S. Minomura and H. Drickamer, *J. Phys. Chem. Solids* **23**, 451 (1962).
- [19] J. C. Jamieson, *Science* **139**, 762 (1963).
- [20] M. Pavlovskii, *Sov. Phys. Solid State* **9**, 2514 (1968).
- [21] W. Gust and E. Royce, *Dynamic Yield Strengths of Light Armor Materials*, Tech. Rep. UCRL-50901 (California Univ., Lawrence Livermore Radiation Lab., 1970).
- [22] W. Gust and E. Royce, *J. Appl. Phys.* **42**, 1897 (1971).
- [23] T. Goto, T. Sato, and Y. Syono, *Jpn. J. Appl. Phys.* **21**, L369 (1982).
- [24] S. J. Turneure and Y. Gupta, *Appl. Phys. Lett.* **91**, 201913 (2007).
- [25] S. J. Turneure and Y. Gupta, *Appl. Phys. Lett.* **90**, 051905 (2007).
- [26] M. I. McMahon, R. J. Nelmes, N. G. Wright, and D. R. Allan, *Phys. Rev. B* **50**, 739 (1994).
- [27] G. Mogni, A. Higginbotham, K. Gaál-Nagy, N. Park, and J. S. Wark, *Phys. Rev. B* **89**, 064104 (2014).
- [28] J. Tersoff, *Phys. Rev. Lett.* **56**, 632 (1986).
- [29] J. Tersoff, *Phys. Rev. B* **38**, 9902 (1988).
- [30] P. Erhart and K. Albe, *Phys. Rev. B* **71**, 035211 (2005).
- [31] J. Junquera, O. Paz, D. Sánchez-Portal, and E. Artacho, *Phys. Rev. B* **64**, 235111 (2001).
- [32] J. M. Soler, E. Artacho, J. D. Gale, A. García, J. Junquera, P. Ordejón, and D. Sánchez-Portal, *J. Phys. Condens. Matter* **14**, 2745 (2002).
- [33] J. P. Perdew, K. Burke, and M. Ernzerhof, *Phys. Rev. Lett.* **77**, 3865 (1996).
- [34] N. Troullier and J. L. Martins, *Phys. Rev. B* **43**, 1993 (1991).
- [35] N. D. Mermin, *Phys. Rev.* **137**, A1441 (1965).
- [36] S. C. Harvey, R. K.-Z. Tan, and T. E. Cheatham, *J. Comput. Chem.* **19**, 726 (1998).
- [37] J. J. Hall, *Phys. Rev.* **161**, 756 (1967).
- [38] A. Kubo, Y. Wang, C. E. Runge, T. Uchida, B. Kiefer, N. Nishiyama, and T. S. Duffy, *J. Phys. Chem. Solids* **69**, 2255 (2008).
- [39] R. E. Duff and F. S. Minshall, *Phys. Rev.* **108**, 1207 (1957).
- [40] R. Hull, *Properties of Crystalline Silicon*, EMIS datareviews series (INSPEC, the Institution of Electrical Engineers, 1999).
- [41] <http://www.hpc.cam.ac.uk/>